Local formability and strength of TWIP-TRIP weldments for stamping tailor welded blanks (TWBs)

Local formability and strength of TWIP-TRIP weldments for stamping tailor welded blanks (TWBs)

P. Russo Spena[a]*, L. Cortese[b], F. Nalli[a], K. Májlinger[c]

[a]Free University of Bozen-Bolzano, Faculty of Science and Technology, Piazza Università 5, 39100 Bolzano, Italy
[b]Department of Mechanical and Aerospace Engineering, Sapienza University of Rome, Via Eudossiana 18, 00184, Roma, Italy.
[c]Department of Materials Science and Engineering, Budapest University of Technology and Economics, Bertalan Lajos str. 7, H-1111 Budapest, Hungary.

pasquale.russospena@unibz.it, http://orcid.org/0000-0003-0307-2344
luca.cortese@uniroma1.it, http://orcid.org/0000-0002-2959-1014
filippo.nalli@natec.unibz.it
vmkornel@eik.bme.hu, http://orcid.org/0000-0002-6878-1611

***Corresponding author, Pasquale Russo Spena**
Faculty of Science and Technology, Free University of Bozen-Bolzano,
Piazza Università 5, 39100 Bolzano (Italy)
pasquale.russospena@unibz.it

Abstract

The assessment of the local formability and mechanical behavior of weldments in tailor welded blanks (TWBs) made of advanced high strength steels is of crucial importance in the automotive industry, both for the mechanical design of tailored components, and to set up accurate sheet forming numerical simulations. This work investigates the formability of TWBs made of a twinning induced plasticity (TWIP) and transformation induced plasticity (TRIP) steel, determining the local elasto-plastic behavior of the different regions of the weldment. To this purpose, several micro-samples were extracted along the weld seam and heat affected zones, and then subjected to tensile tests. Tensile tests were also performed on macro-samples to assess the overall mechanical behavior of the TWBs during plastic deformation. A digital image correlation (DIC) technique was used to measure the surface strain field of both micro- and macro-samples, to calculate the plastic strain ratio, through-thickness strain, and to point out possible inhomogeneities in plastic behavior of the TWB weld beads. The TWB joint exhibited a significant formability of the fusion zone and of the TWIP heat affected zone, whereas it was rather limited at the TRIP side. Locally, an uneven plastic behavior within the fusion zone was observed, with a variable plastic strain ratio (i.e. thinning) in both axial and transverse direction. The other regions of the weld, instead, deformed more homogenously. Preliminary considerations about the numerical modeling of TWIP/TRIP TWBs and their prospective use in sheet forming operations have been outlined.

Keywords: Advanced high strength steels; tailor welded blank; local mechanical characterization; sheet forming; FE analysis; automotive applications.

Acknowledgments

The authors are grateful to the Free University of Bozen-Bolzano that has supported part of this research (title project: “Tailor welded blanks of aluminum alloys and steels for the fabrication of automotive lightweight components”; scientific coordinator: dr. P. Russo Spena). This work has been also supported by the János Bolyai Research Scholarship of the Hungarian Academy of Sciences grant number: BO/00294/14 and by The Hungarian Research Fund, NKTH-OTKA PD 120865 (dr. K. Májlinger).

1. Introduction

Advanced high strength steel (AHSS) sheets are widely used to fabricate a variety of car body parts in the automotive industry. In some cases, already shaped components are assembled together using different fusion welding techniques, such as resistance spot welding, arc and laser welding. Shome and Tumuluru [1] have given an overview about the welding techniques used to join AHSSs, also pointing out crucial challenges and future trends. Other studies have focused on more specific aspects of joining of AHSS sheets. Russo Spena et al. [2, 3] investigated the effects of the main welding parameters on spot weld quality of quenching and partition (Q&P), TWIP and TRIP steel sheets, determining proper weldability windows. Májlinger et al. [4] focused on gas metal arc welding of TWIP and TRIP steels, evaluating the influence of welding parameters on joint quality, and mechanical and microstructural properties of weld seams. Mazar et al. [5] investigated the employment of hybrid laser/arc welding and transition inserts to join AHSS steels with aluminum alloys. Other studies focused on other high strength steel grades [6-9]. In other cases, laser or arc welding are used to join steel sheets into a single blank (tailor welded blank, TWB), which is typically made from sheets with different alloying elements, thicknesses, coatings or material properties. After joining, it is subjected to stamping or deep drawing. The automotive sector has been developing an increasingly interest in TWBs because they offer a huge flexibility in designing lightweight components: different steel grades or thicknesses can be employed to fabricate tailored multi-material parts for specific aims. This is helpful to optimize material distribution in the final component, allowing to save materials, reduce costs in forming operations and assembling, fabricate lighter parts, as well as to enhance crashworthiness because of an improved strength and stiffness. However, stamping of a tailored component is more critical than that of a uniform blank because it involves the plastic deformation of a welded sheet with inhomogeneous mechanical properties [10-14]. This is due to the presence of different steel grades and thicknesses, as well as of one or more weldments, which usually have a reduced ductility. The weld mechanical properties are strongly affected by the heat input provided during the joining process because it alters significantly the microstructures of the parent materials. More specifically, the joined sheet edges are completely melted (i.e. fusion zone, FZ), while the surrounding unmelted regions undergo an intense heating (i.e. heat affected zone, HAZ). As a result, the microstructure, mechanical strength, and formability of the welded joints are remarkably different from those of the parent materials. Moreover, the microstructural transformations and volumetric changes of the weldment during the heating and final cooling may give rise to significant residual stresses, improper microstructures and/or of defects (e.g. cracks, incomplete penetration, and

pores) often both at a microscopic and macroscopic scale. All these features reduce further the capability of a TWB to cope with large plastic deformation during sheet metalworking. This is particularly true for AHSSs because of their peculiar microstructures and mechanical properties, which are obtained following strict thermo-mechanical rolling processes, are completely destroyed and altered by the welding process.

Several HSS and AHSS grades are currently employed to fabricate tailored components, including high strength low alloy (HSLA) steels, DP and TRIP steels. Recent studies have aimed at investigating the use of more performing AHSSs, such as TWIP steels. These steel grades exhibit exceptional combinations of strength and ductility. TWIP are austenitic steels with a medium or high content of manganese (10-25 wt.%) and a variable carbon content (0.05-0.60 wt.%). The ultimate tensile strength of TWIP steels generally exceeds 900 MPa with elongations at fracture over 40 %. Currently, the use of these steels is restricted to prototypes and a very few structural components, whereas there are no applications as TWB components. This is mainly due to the quite limited studies about dissimilar welding of TWIP steels, as well as to some issues related to the fabrication of zinc-coated TWIP sheets and to liquid metal embrittlement. In this context, Kang et al. [15] pointed out the detrimental effect of Zn metal embrittlement in fracture resistance of hot dip Zn-coated TWIP steels, whereas Beal et al. [16] evaluated the effect of temperature, strain rate and pre-exposure time on the occurrence of embrittlement in Zn-coated TWIP specimen using a Gleeble® thermo-mechanical simulator. Previous studies focused on laser welding of TWIP steels. Rossini et al. [17] studied the mechanical properties of dissimilar laser joints of TWIP steels with other AHSSs, such as TRIP and hot stamping boron steels. They pointed out the detrimental effects of welding TWIP to other steels (e.g. DP, TRIP, 22MnB grades) without the use of proper metal fillers. Wang et al. [18] investigated in more detail the microstructure and mechanical properties of the FZ of TWIP laser joints. This study emphasized that the FZ had a yield strength similar to the base metal, but an ultimate tensile strength and an elongation at fracture about 20 % and 50 % lower, respectively.

There are few studies about sheet forming of TWB made of TWIP steels. Nguyen et al. [19] set a tool design in combination with optimized process parameters to improve the deep drawability of a TWB made of TWIP and mild steels. In a following study, Nguyen et al. [20] reduced the springback of these TWBs through a genetic algorithm based on a multi-objective optimization technique. All the above-mentioned studies and other researches have not generally considered the influence of weldments during plastic deformation of TWBs, if not with rough approximations, since the mechanical and formability properties of the welded regions are almost always unknown.

This is why these studies are generally based on standard forming tests that, even if they can be used to assess the formability of TWBs as a whole, do not focus on forming mechanics of weld lines and surrounding HAZ regions. The uncertainties in predicting the mechanical response of TWBs lead to design these tailored blanks in a way to reduce as much as possible the state of stress in the welded region during sheet forming, concentrating the intense stresses and deformations in the more ductile base materials. A better design based on an accurate knowledge of the local formability of TWB weldments would allow to fabricate more complex, lighter and/or with an improved functionality tailored parts, while maintaining important requirements like crashworthiness and cutting down stamping wastes.

Laser welding is commonly used for the fabrication of TWBs made of current automotive steel grades. However, laser welding suffers chiefly from the difficulty to manage the coupling of laser beam and filler metal in an automatized industrial welding line. In this case, plasma and arc welding are preferred when metal fillers are mandatory to join sheets into a single blank. In this regard, since a metal filler is mandatory in dissimilar welding of TWIP to other automotive steel grades, plasma and arc welding should be considered as the more appropriate technologies for the future development of TWBs made of these steel grades.

This research focuses on an accurate local and global characterization of arc-welded TWBs made of TWIP and TRIP steel sheets with the aim of i) establishing the feasibility of TWIP/TRIP tailored car components and ii) providing helpful data for an accurate FE simulation of TWB stamping and mechanical design. More in detail, the elasto-plastic behavior of the base materials and of the weld seam regions have been determined at a macroscopic and local level to assess the mechanical response of these different zones in terms of strength and formability. This has been accomplished through tensile tests that were executed on micro- and macro-specimens cut from the FZ and the HAZs of the welded joints. Additional local data have been provided with the aid of a white light speckle digital image correlation (DIC) measurement technique based on the study of Broggiato and Cortese [21], which was employed during all tests to retrieve the full displacement and strain field on the samples surface. This information has been used for a deeper understanding of the formability of the different regions of the TWBs, evaluating through-thickness strain and plastic strain ratio of the micro-samples and possible inhomogeneities in their elasto-plastic behavior during the tensile tests, as well as to detect welding defects.

Overall, prospective advances in the design of actual TWB forming processes are pointed out. It is worth noting that the local stress-strain curves identified in this work could be also profitably employed in conventional and advanced

plasticity material models, similarly to what was done by Broggiato et al. [22], to be used in finite element (FE) simulations of TWB stamping processes. In this way, these software tools would include a more accurate local description of the mechanical response of the welded regions.

2. Materials and Experiments

A zinc coated TRIP and a TWIP steel sheet were used to realize the TWBs, respectively with a thickness of 0.9 mm and 1.4 mm. The apparent grain size of the two steel microstructures (as an average size of all the metallurgical constituents) has been measured according to the EN ISO 643 standard [23]. TWIP and TRIP steel were joined by means of gas metal arc welding (GMAW). An AWS ER 307 Si wire with a diameter of 0.8 mm was employed as consumable electrode. Table 1 lists the chemical composition of the two steels (obtained from emission spectrometry) and of the consumable electrode (nominal composition).

Table 1. Chemical composition of the TWIP and TRIP steels and nominal composition of the filler wire.

Steel	*Alloying element (wt.%)*								
	C	Si	Mn	Al	Ni	Cr	Fe	Cr_{eq}	Ni_{eq}
TWIP	0.51	0.46	17.5	1.00	-	0.13	bal.	1.6	22.8
TRIP	0.27	1.52	2.10	0.25	-	-	bal.	2.3	9.15
AWS307	0.08	1.45	6.62	-	9.03	19.1	bal.	21.3	14.7

The TWBs were realized by butt welding 300 mm ×150 mm TWIP and TRIP sheet coupons. The sheets were clamped on the same plane and then welded using a Rehm Mega PULS 300 GMAW machine automated with a Yamaha linear drive. The welding torch was perpendicular to the sheets (the thickness step of the sheets was on the torch side) during the joining process. The main welding parameters were: voltage 16.4 V, amperage 30 A, wire feed rate of 3.5 $m \cdot min^{-1}$, polarity DC+ (direct current wire positive), welding speed 2.74 $mm \cdot s^{-1}$. An argon shielding gas was insufflated on either sides of the bead with a flow rate of 10 $l \cdot min^{-1}$, the gap was 1 mm, the torch distance 10 mm. Preliminary pilot welding tests were conducted to assess proper welding parameters, and to ensure a full weld penetration and the absence of defects (e.g. cracks, pores or excess of penetration). Optical and SEM microscopy examinations were carried out throughout the weld seams, from the base materials to the bead, to examine all the different microstructures. Microstructure investigations were conducted on standard metallographic

samples extracted from the cross section of the welded joints. Different etchants were used for the two steel grades and joint parts: Le Pera (100 ml H_2O + 1 g $Na_2S_2O_5$, 100 ml ethanol + 4 g $C_6H_3N_3O_7$) etching for TWIP steel and TWIP HAZ; Marder & Benscoter (100 ml H_2O + 10 g $Na_2S_2O_5$, pre-etching with nital 2 vol%) or nital (3 vol% HNO_3 in ethanol) etching for TRIP steel, FZ and TRIP HAZ. In the same regions, Vickers microhardness tests with a load of 200 g (HV0.2) and a holding time of 10 s were performed according to the ASTM E384 standard [24].

Regarding the local characterization of the different regions of the joints, several flat tensile micro-specimens were extracted from the FZ and the HAZs of the TWIP and TRIP steels by electrical discharge machining. Specimens size was chosen sufficiently small to be representative of the local behavior of the zones they were extracted from, but large enough to remain in a macroscale domain. The most suitable positions were chosen based on a microstructural examination and microhardness profiles, as discussed thereafter. The extraction scheme of micro-samples is reported in Fig. 1. After machining, they were ground accurately to obtain an even cross section throughout the whole length (resulting in a 0.9 mm final thickness), avoiding any significant heating that could alter the sample microstructures. Figure 2a shows the size of the micro-samples.

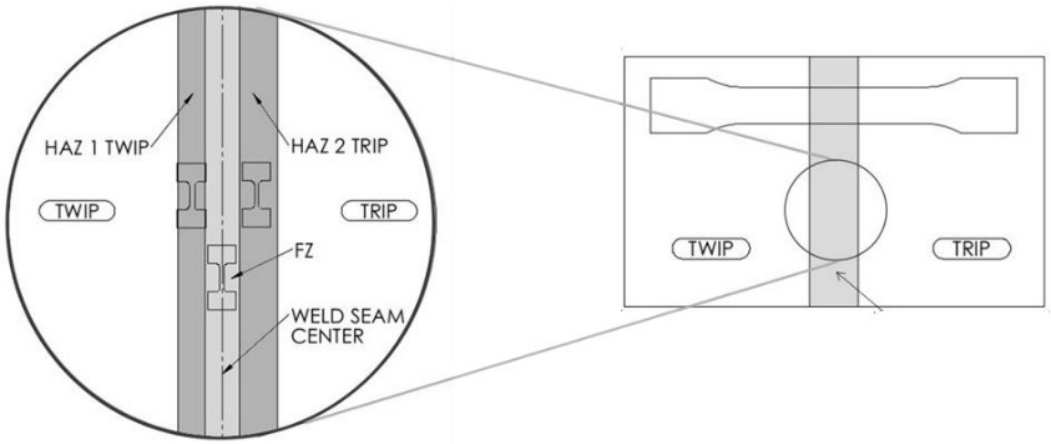

Fig. 1. Schematic drawing of the welded TWIP/TRIP coupon with the extraction positions of all specimens. Drawings not to scale.

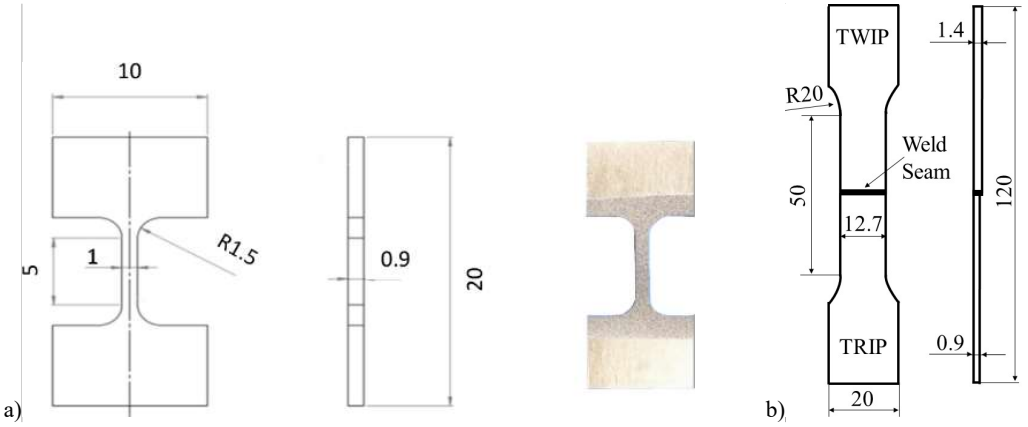

Fig. 2. a) Micro-specimen and b) macro-specimen size. All the dimensions of the drawings of image a) and b) are in "mm". Drawings not to scale.

Micro-samples were subjected to tensile tests in compliance with the ASTM E8M standard [25]. Custom-made micro-grips mounted on a 250 kN hydraulic MTS machine were used to clamp the sample ends. Crosshead speed was set to 0.25 mm/min, while a 2 kN HBM load cell and an Epsilon 3542 extensometer with a 25 mm gauge length were used to acquire load and displacement data. The extensometer had to be set on the gripping system itself, rather than on the gauge section, due to its extremely limited length (5 mm). In data post processing phase, the unusual placement has properly been taken into account. During the tensile tests, digital images were captured using a Nikon D7100 SRL camera equipped with a 60 mm micro Nikkor lens, mounted on a frame rigidly connected to the testing machine. Images were post-processed using a white light DIC speckle algorithm to measure the displacement and strain fields on the sample surfaces.

To assess the global elasto-plastic behavior of the TWB joints, dog-bone specimens were cut throughout the welded sheet, encompassing the base materials, HAZs and the FZ, with the weldment in the middle of the gauge section and perpendicular to the specimen axis, refer to Fig. 1 and Fig. 2b. The gauge width and length were 12.7 mm and 50 mm, respectively. The original thicknesses of the TWIP and TRIP joined sheets were kept unchanged. Standard tensile tests were also carried out to characterize the TWIP and TRIP base materials.

3. Results and Discussion

3.1 Microstructure and Vickers microhardness

TWIP steel exhibits a fully austenitic microstructure, Fig. 3a, while TRIP steel shows a mixed microstructure made of retained austenite, ferrite and bainite, Fig. 3b. The average apparent grain sizes of TWIP and TRIP steels are about 5 μm and 3 μm, respectively.

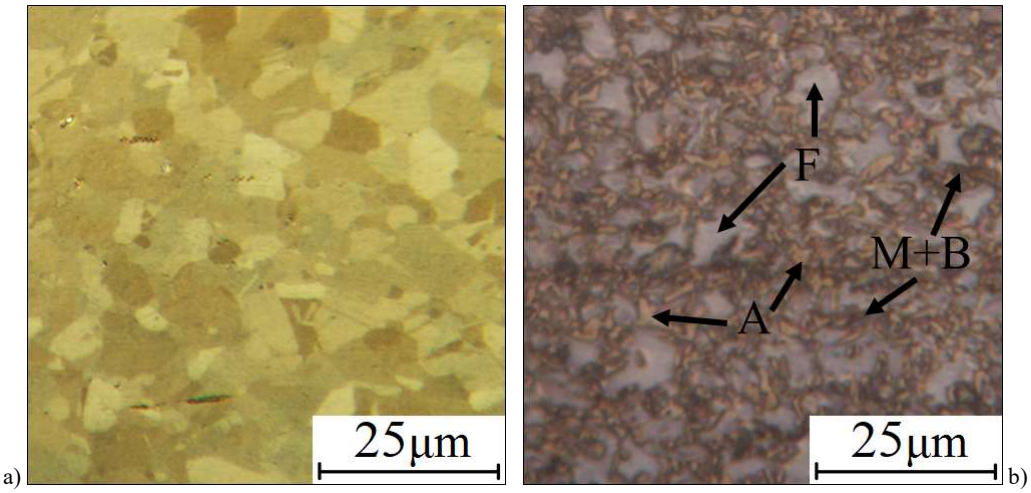

Fig. 3. SEM micrographs of the examined steel grades: a) TWIP (Le Pera etching) and b) TRIP steels (Marder & Benscoter etching). A: austenite; F: ferrite; M+B: martensite and bainite.

A stereomicroscope image of the cross section of a TWB joint and some optical micrographs obtained from different zones of the weld bead can be seen in Fig. 4. The same figure shows the locations (indicated with red squares) where the micro-samples were extracted. Overall, the welded joints did not exhibit any macroscopic defects and the weld beads were evenly distributed between the two steel sheets. The FZ is fully austenitic (because of the filler chemical composition) and shows large grains with an uneven size and the typical dendritic solidification pattern. Its width is about 7 mm. The HAZ at the TWIP side remained fully austenitic after the welding process, its width is about 2.5 mm. It exhibits coarse grains close to the FZ and a grain recrystallization farther away. At the TRIP side, the HAZ consists of martensite next to the FZ: this region austenitized during the joining process and then cooled rapidly, thus promoting the formation of such phase. TRIP steel did not transform into austenite away from the FZ, where

instead previous ferrite softened, bainite tempered, and retained austenite tended to transform into bainite. In this case, the width of the HAZ is about 5 mm.

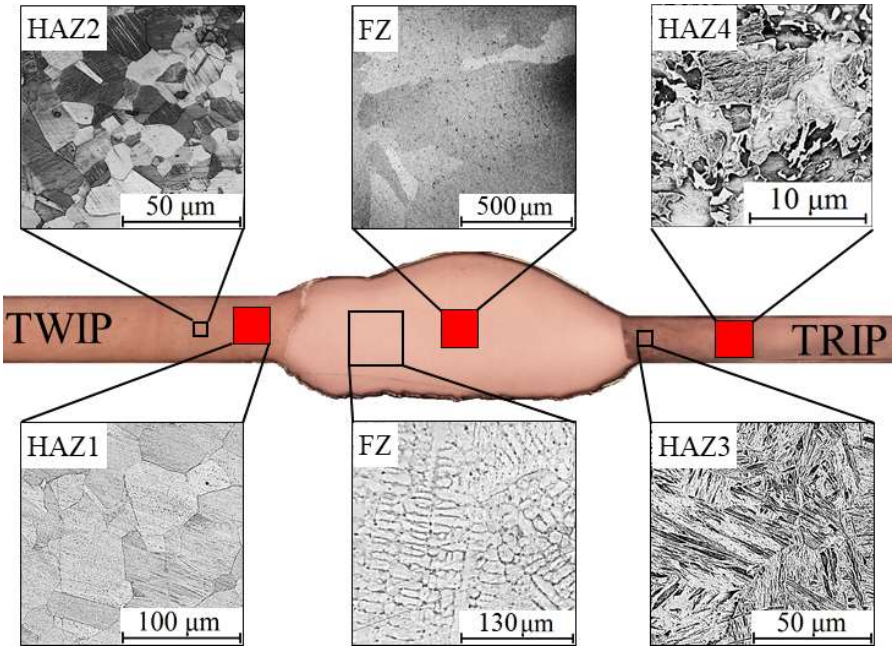

Fig. 4. Cross section and microstructures of a TWIP/TRIP TWB joint. The red squares indicate the locations of the micro-samples extraction. Nital etching used for the FZ and TRIP HAZ; Le Pera etching used for the TWIP HAZ.

The hardness of TWIP steel is about 240 HV0.2, while that of TRIP steel is 235 HV0.2. Fig. 5 shows a hardness profile of the investigated TWB weldments. The FZ has a hardness in a 180-220 HV0.2 range due to the fully austenitic microstructure present in this region. The scatter of hardness values in this region can be mainly attributed to a local inhomogeneous dilution of the filler wire with the two steels, chemical segregation, and the dendritic microstructure, which are typical of filler welded joints. Based on the hardness profile, the microstructure of TWIP steel is unaffected beyond about 2.5 mm from the border of the FZ, and beyond 5 mm for TRIP steel. This is coherent with the microstructural examination. The HAZ of TWIP steel has a lower hardness than the base material. This is mainly due to the grain coarsening close to the FZ (refer to HAZ1 of Fig. 4). At the TRIP side, the martensitic microstructure (refer to HAZ3 of Fig. 4) exhibits a hardness of about 440 HV0.2 close to the FZ. The weld bead hardness reduces in the HAZ where a full austenitization did not occur, coherently to the phase transformations described previously.

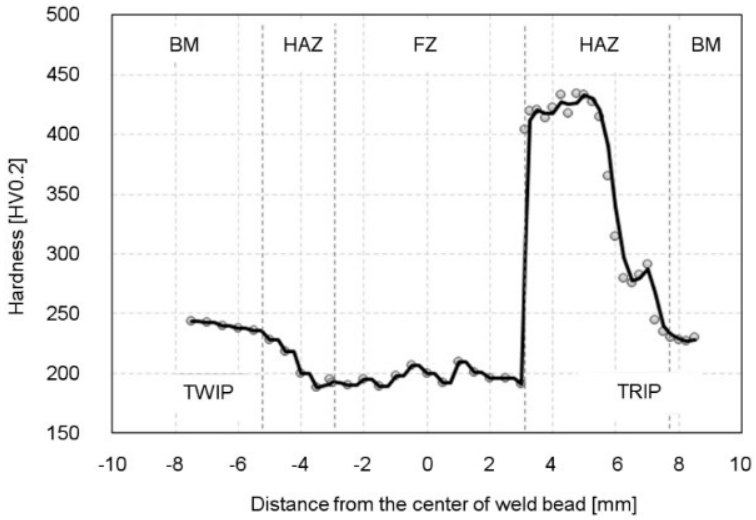

Fig. 5. Vickers microhardness profile obtained through the cross section of the TWIP/TRIP TWB joint.

3.2 Micro-sample tests: TWB local characterization

The engineering stress-strain curves obtained from the tensile tests of TWIP and TRIP steels are illustrated in Fig. 6. TWIP steel exhibits an ultimate tensile strength of 1030 MPa, an elongation at fracture of about 50 %, and a strain hardening exponent (coefficient n of the Hollomon equation $\sigma = K\varepsilon^n$) of 0.30. TRIP steel has a UTS of 960 MPa, an elongation at fracture of 23 %, and n equal to 0.24. TWIP and TRIP steels did not show a significant necking, such that the tensile samples always fractured close to the maximum load. As reported in the datasheet, the filler metal AWS 307 had a nominal tensile strength of 590 MPa and an elongation at fracture of 35 %.

The tensile properties of the micro-samples are also reported in Fig. 6. The samples extracted from the FZ and the HAZ1 at the TWIP side show a large elongation at fracture, coherently with the fully austenitic microstructures of these regions. The grain size at the TWIP side has a notable influence on mechanical strength and ductility. The larger grains in the HAZ1 region triggered the onset of plastic deformation at lower stresses than the base materials. This can be clarified based on the relationship $\sigma_y = \sigma_0 + K\, d^{0.5}$ based on the studies of Hall [26] and Petch [27], where σ_y is the yield strength, σ_0 is the resistance of the lattice to dislocation motion, K is the strengthening coefficient, and d the initial average grain diameter. The higher ductility of the HAZ1 region is ascribed to the positive effect of grain size in increasing elongation at fracture promoted by the twinning effect. As reported by Gutierrez-Urrutia and Raabe [28] , dislocation glide mainly controls plasticity in TWIP steels in the early deformation stages, whereas the average dislocation cell size and twin spacing govern plastic deformation at

intermediate-high levels. In this context, even though large grains drive the onset of plastic deformation at a lower yield strength and a less intense work hardening than finer microstructures, the more numerous twins substructures that form in large grains during plastic deformation are able to postpone the final fracture to higher elongations. The samples extracted from the HAZ at the TRIP side exhibit a high ultimate tensile strength and a limited elongation at fracture coherently with their fully martensitic microstructure. The engineering stress-strain curves obtained from micro-samples are consistent with the hardness values of the regions where they were extracted from.

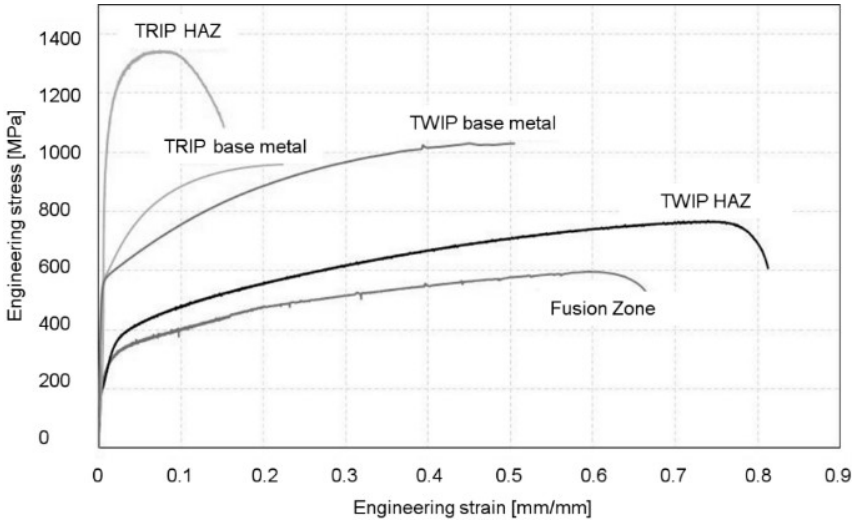

Fig. 6. Engineering stress-strain curves obtained from the tensile tests performed on base steels and the micro-samples extracted from the TWB weldments.

Table 2 reports the ultimate tensile strength, strain hardening exponent, and elongation at fracture of the fusion and heat affected zones. Three independent methods were employed to evaluate the elongation at fracture: a manual measurement of the initial and fractured gauge length using a caliper; the measurement taken with the extensometer; the calculation from the displacements of the end edges of the gauge length as obtained from the DIC analysis.

Table 2. Ultimate tensile strength (UTS), elongation at fracture, and strain hardening exponent of the fusion and heat affected zones. Elongation at fracture was obtained independently by direct measurement, extensometer, and DIC analysis. All the values reported are the average of at least two tests performed for each joint area.

Joint area	UTS [MPa]	Hardening exponent n [-]	Average elongation at fracture [mm/mm]			
			Measured	DIC	Extensometer	Average
TWIP HAZ	854	0.29	0.76	0.78	0.80	0.78
FZ	655	0.29	0.68	0.75	0.66	0.70
TRIP HAZ	1430	0.19	0.18	0.14	0.15	0.16

For the usage of elasto-plastic isotropic models in FE stamping simulations, the true stress-strain curves were calculated for both base metals and all the weldments zones from engineering data. They are reported as dark grey curves in Fig. 7. These curves have been extended to large strain (light grey curves in Fig. 7) using the Voce's non-linear relationship $\sigma = \sigma_y + A(1-e^{-be})+C\varepsilon$, commonly adopted in FE codes. In the expression, σ_y is the yield stress and *A, b, C* three material constants to be calibrated. These parameters have been identified by an inverse method based on FE models reproducing the actual tensile tests, looking for the best match between experiments and numerical simulations, in terms of load-displacement curves. The commercial code Ansys has been used to this purpose. The resulting best fit sets are summarized in Table 3.

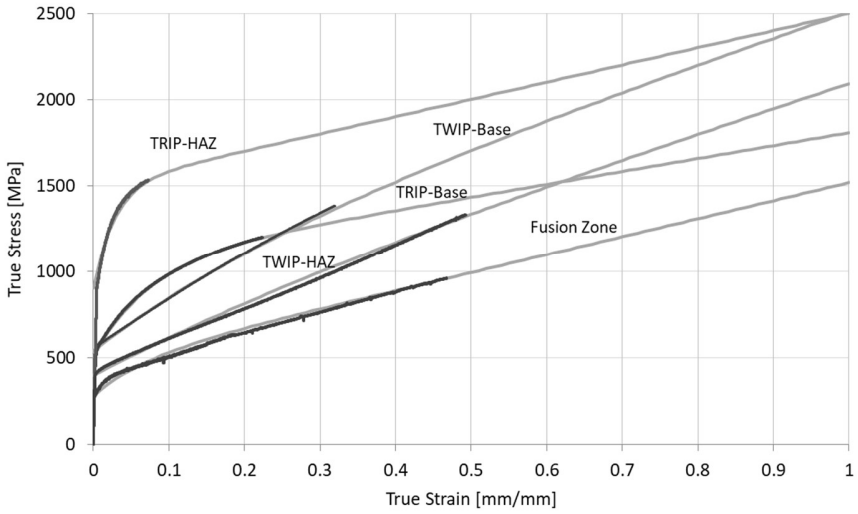

Fig. 7. True stress-strain curves of the base metals and different regions of TWB weldment (dark grey) extended to large strain (light grey), as obtained through an inverse FE method.

Table 3. True stress-strain curves: best fit parameters of the Voce's non-linear relationship.

		TRIP Base	TWIP Base	WELD-SEAM	HAZ-TWIP	HAZ-TRIP
σ_y	[MPa]	510	540	280	400	903
A	[MPa]	550	480	190	290	600
b	[-]	13	4	15	3	35
C	[MPa]	750	1500	1050	1420	1000

The DIC analysis allowed to calculate the strain field on the gauge surface at increasing loads for the FZ and HAZ regions and to detect possible strain concentrations or gradients related to material inhomogeneities induced by the welding process. It was also used to retrieve through-thickness strain and plastic strain ratio to evaluate the local formability of TWB weldments. Figs. 8-10 show some contour maps of the total equivalent strain of the FZ and HAZ at the TWIP and TRIP side. In each figure, the three snapshots correspond to different increasing loads, as indicated in the captions. Colors are repeated in the contour maps to enhance the resolution and the identification of the strain gradients. It can be noticed how the HAZ regions exhibit a rather homogeneous plastic behavior, even after the strain localization at the highest loads caused by the onset of necking. On the contrary, the FZ shows a non-uniform plastic behavior. Localized strain gradients occur since the beginning of the test, and then they become more and more intense as the applied load increases. Regardless the weld region examined, this phenomenon was observed systematically for all the micro-samples. It can be attributed to the intrinsic chemical and microstructural inhomogeneity of the FZ.

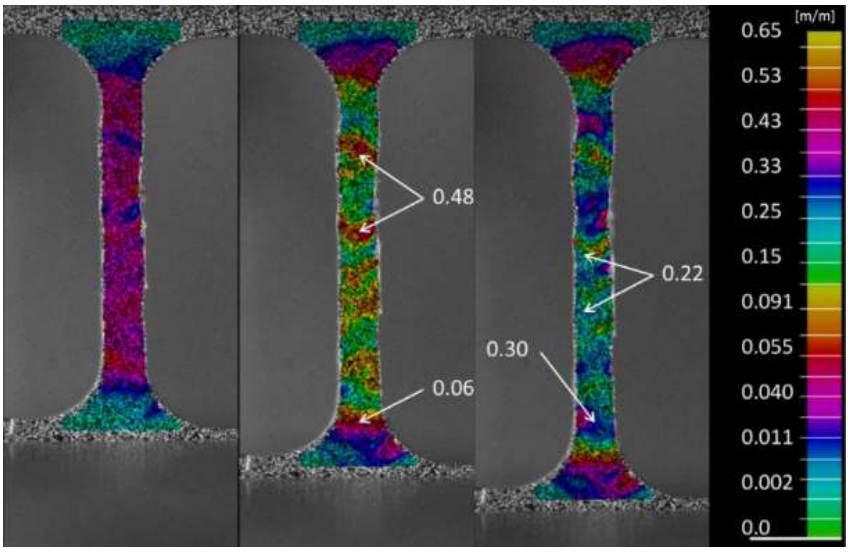

Fig. 8. FZ micro-specimen tensile test. Total equivalent strain at four load levels (and nominal stresses): 0.52 kN (578 MPa), 0.58 kN (645 MPa), 0.60 kN (667 MPa).

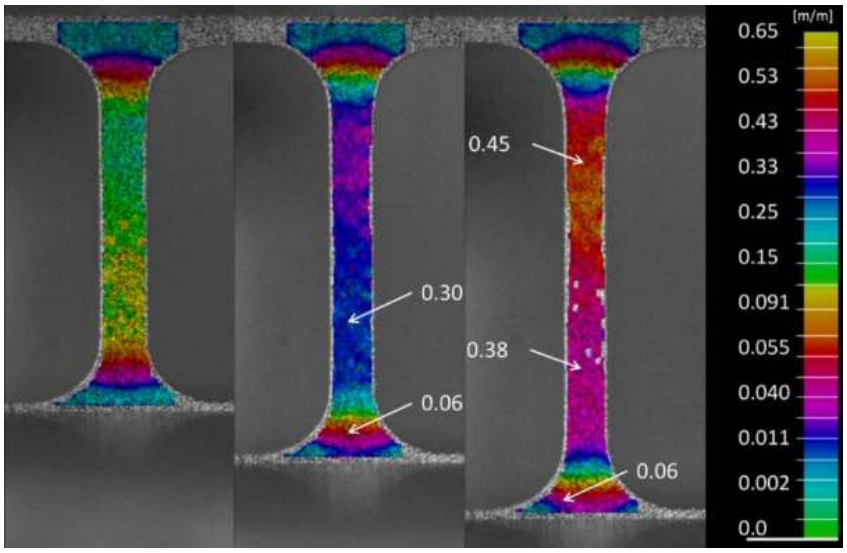

Fig. 9. TWIP HAZ micro-specimen tensile test. Total equivalent strain at four load levels (and nominal stresses): 0.59 kN (655 MPa), 0.70 kN (778 MPa), 0.76 kN (845 MPa).

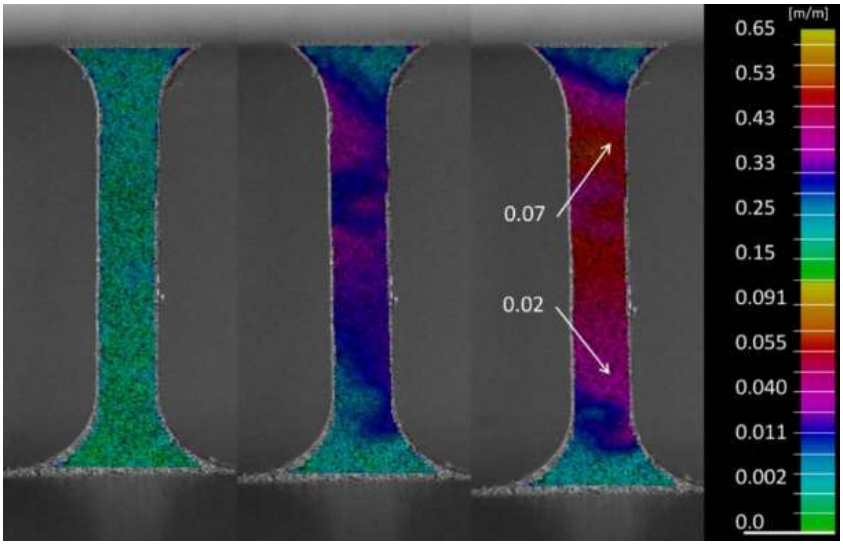

Fig. 10. TRIP HAZ micro-specimen tensile test. Total equivalent strain at four load levels (and nominal stresses): 0.42 kN (467 MPa), 1.20 kN (1334 MPa), 1.30 kN (1445 MPa).

The drawability of a TWB is mainly governed by the ability of the sheets and of the weldment to resist thinning when subjected to in-plane tensile stresses. This feature can be quantified in terms of plastic strain ratio. Plastic strain ratio is considered a direct measure of normal anisotropy being defined as the ratio of the true strain in the

transverse direction and the true strain through the thickness under tension. The through-thickness strain is calculated from the in-plane strains based on the constancy of the volume. These data are usually calculated from global quantities measured on a sheet sample (initial and final width, length and thickness) during a tensile test. DIC allows to collect more reliable values of the through-thickness strain and normal anisotropy of the micro-samples, and also to measure the evolution of these factors during a tensile test. Figs. 11-13 show the total equivalent strain, through-thickness strain, and plastic strain ratio evaluated for the FZ and HAZs micro-samples, at the higher load levels of Figs. 8-10. Data are plotted using a six level contour map to emphasize the extent of the zones with a different plastic behavior. Overall, the distributions of the through-thickness strain are consistent with the equivalent plastic strain maps. Concerning the FZ specimen, an inhomogeneous spatial distribution of the through-thickness strain and plastic strain ratio is observed throughout the sample. Particularly, the plastic strain ratio ranges from 0.5 to 1.9. This put into evidence the difficulty to control the thinning of the weldment during a sheet forming operation and its modeling in numerical simulations. Smoother transitions and narrower ranges instead characterize the local behavior of the HAZs at the TWIP, Fig. 12, and TRIP side, Fig. 13. The larger deformation of the upper part of the TWIP HAZ micro-sample (orange region) is due to necking and must not be confused with a non-uniform material behavior.

Since plastic strain ratio refers to a uniaxial loading condition, the presented measures are only meaningful in the regions of the specimens not affected by necking (where the stress state is multiaxial). Particularly, the plastic strain ratio decreases significantly at the beginning of plastic deformation, then it almost remains constant when plastic deformation increases further. The same trend was found by De Cooman et al. [29] for a Fe-18%Mn-0.6%C-1.5%Al TWIP steel.

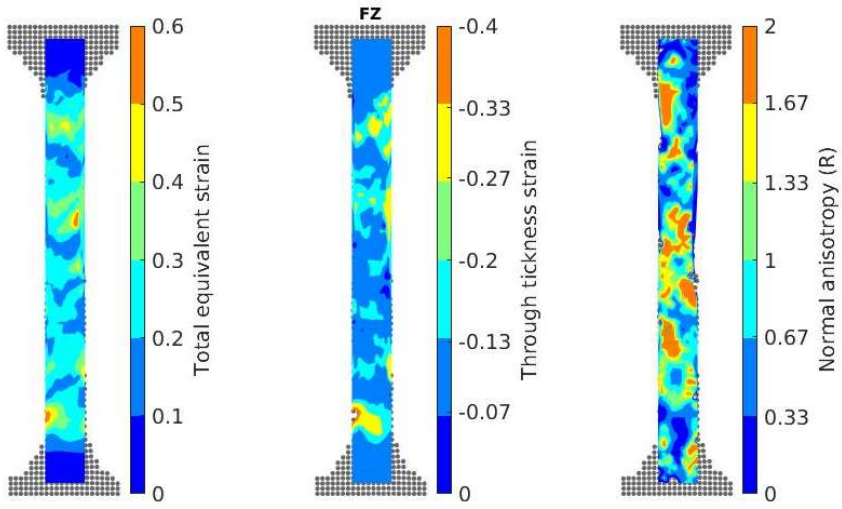

Fig. 11. FZ micro-specimen: total equivalent strain, through-thickness strain, and normal anisotropy (i.e. plastic strain ratio). 0.60 kN load level.

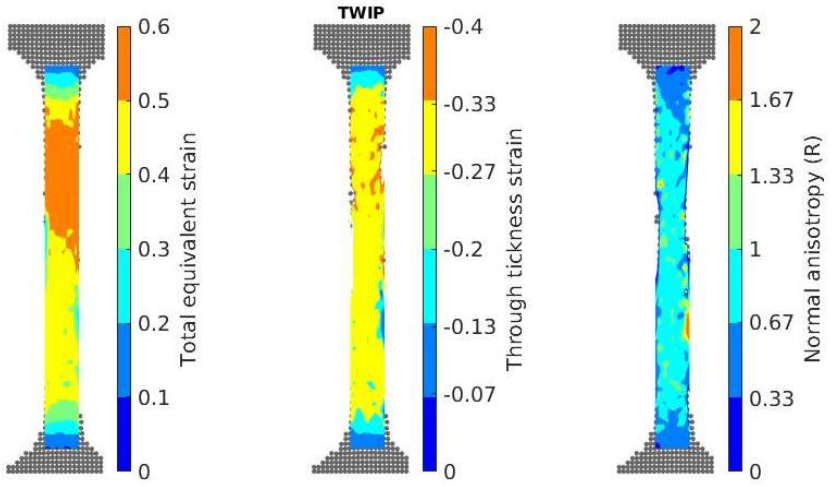

Fig. 12. TWIP HAZ micro-specimen: total equivalent strain, through-thickness strain, and normal anisotropy (i.e. plastic strain ratio). 0.76 kN load level.

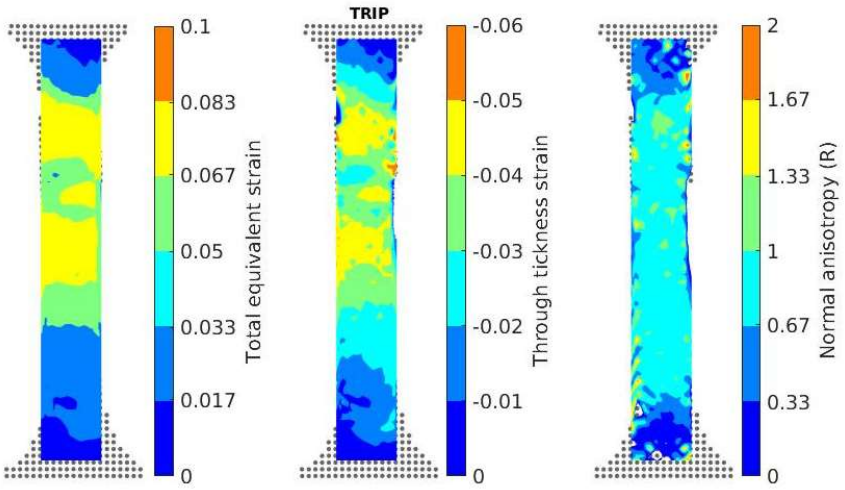

Fig. 13. TRIP HAZ micro-specimen: total equivalent strain, through-thickness strain, and normal anisotropy (i.e. plastic strain ratio). 1.30 kN load level.

The TRIP HAZ shows a more homogeneous plastic deformation throughout the micro-samples than the other regions of the weldment, Fig. 13. This is attributed to the high mechanical strength caused by the presence of bainitic and martensitic structures, which also reduce the total equivalent (in the range of 0 to 0.1 at 1.30 kN load level) and through-thickness strain (in the range of 0 to -0.06 at 1.30 kN load level). Larger deformations are instead observed in the FZ and TWIP HAZ at lower load levels, Figs. 12 and 13. The plastic strain ratio in the TRIP HAZ is in the 0.76-1.0 range, consistently with the literature about similar TRIP steel grades.

3.3 Macro-sample tests: TWB overall characterization

The overall strength of the TWIP/TRIP joint was assessed through tensile tests on the macro-specimens machined from the welded coupon. The resulting load-displacement curves are shown in Fig. 14. A good accordance in terms of global load-displacement curves can be observed among all the repetitions, even though the scatter of the elongation at fracture values is appreciable. This can be interpreted as a positive repeatable mechanical performance of the joint. However, the presence of local imperfections and/or defects lead to a variability in ductility and, hence, in formability of the whole joint. A metallographic etching, which was carried out on all the cross-sections of the fractured samples (Fig. 15a), points out that the macro-specimens always fractured within the FZ nearer the TWIP side, Fig. 15b. A thickness irregularity is clearly visible throughout the weld: the HAZ of TRIP steel remains thicker than the rest of the welded joint, with the major and uneven thinning being in the FZ. This phenomenon is ascribed

to the different mechanical response of the different regions of the joints, coherently with the results obtained from the DIC analysis performed during micro-samples testing (refer to Figs. 8-10).

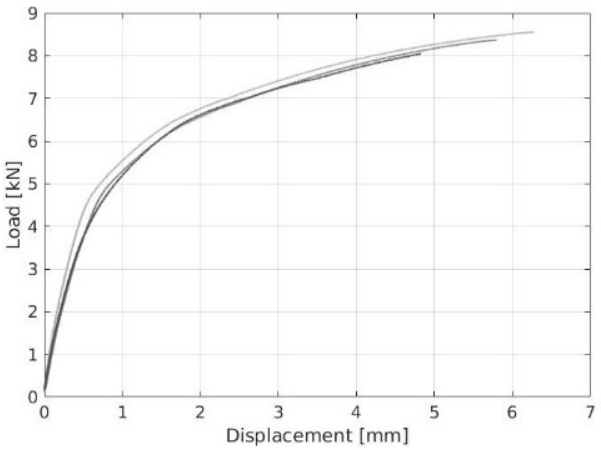

Fig. 14. Load–displacement curves obtained from the tensile test conducted on welded macro-samples.

a)

b)

Fig. 15. a) Macro-specimens after a tensile test run; b) Etched cross-section of a fractured macro-sample. Nital etching used for image b).

DIC results were also used to provide information on how much the weld seam of a TWIP-TRIP TWB is exploited in a forming process with respect to the surrounding base materials. It would be desirable that both the base materials and the weld seams have a similar mechanical behavior during sheet forming to reduce the occurrence of strain and stress gradients, which primarily arise at the interface of the different joints regions. In fact, these strain and stress gradients, along with the lower ductility of the weld seam, are the main causes limiting the overall formability of a TWB. In this regard, Fig. 16 shows the contour maps of the total equivalent plastic strain for a macro-sample at four subsequent load stages (6 kN, 7 kN, 8 kN, 8.2 kN), the latter being close to the final fracture. Again, color contours are repeated to highlight the strain gradients. It is worth noting that all the different regions

participate to the plastic deformation to a certain extent. Then, a progressive strain localization in the FZ (nearer the TWIP side) triggers necking, leading to the final fracture of the specimen.

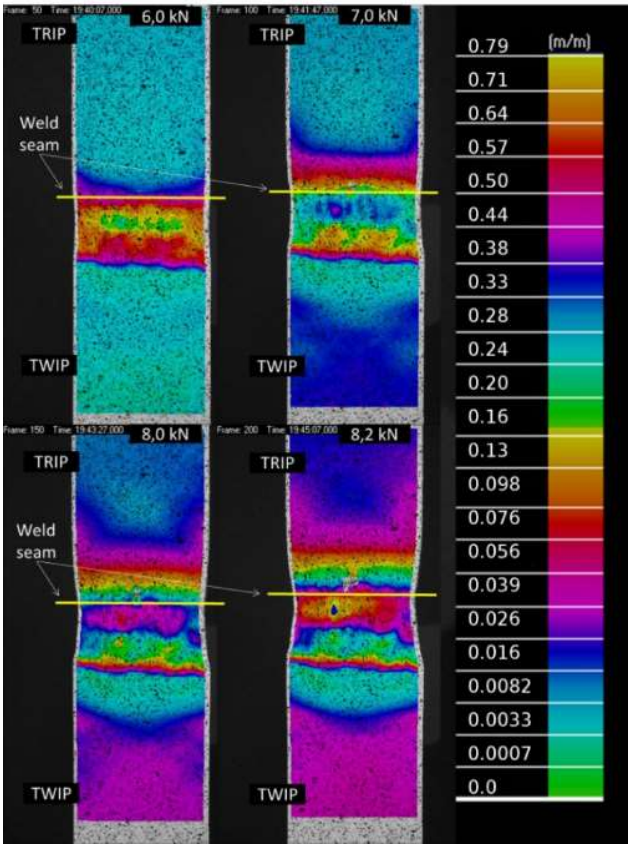

Fig. 16. Total equivalent strain on macro-specimens during a tensile test at four load stages: 6 kN, 7 kN , 8 kN , 8.2 kN. The yellow horizontal lines show the center of the weld seam.

For a further quantification of the results, Fig. 17 shows the equivalent plastic strain levels of the different regions on transversal paths at a given distance from the weld line (highlighted in yellow in Fig. 16), at the highest load level (8.2 kN) of Fig. 16. The graph highlights how the deformations are higher and the overall behavior more inhomogeneous in the FZ than in the rest of the TWBs.

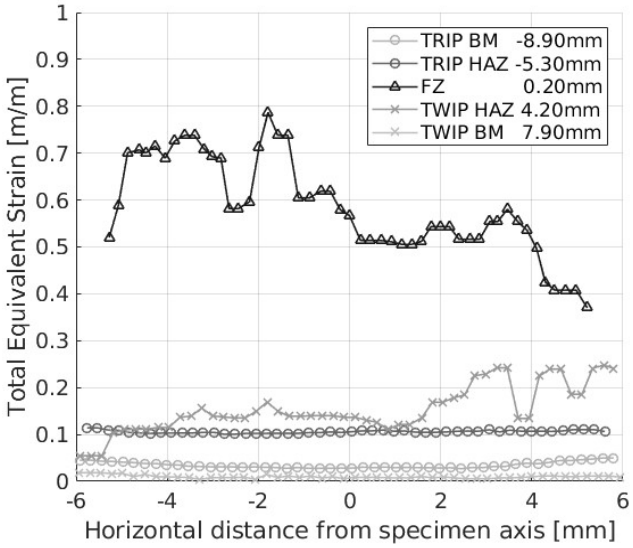

Fig. 17. Equivalent plastic strain on transversal paths for the base metals (BMs), HAZs, and FZ, at 8.2 kN load level. Distances from the weld line are provided in the picture legend.

The deformation of the different regions of the welded joints can be also examined plotting the total equivalent strain, total equivalent strain gradient, and through-thickness strain along a central longitudinal direction, Fig. 18. The origin of the longitudinal path was set in the middle of the weld bead and indicated in the graphs with a solid gray line. Vertical dotted lines are instead used to show the transitions between the FZ and the HAZ regions (inner lines) and between the HAZ regions and the base materials (outer lines). The results are relative to 6 kN, 7 kN, 8 kN, 8.2 kN load stages, as those reported in Fig. 16. Fig. 18a and Fig. 18c show that the FZ region close to the TWIP side exhibits the largest strain and thinning, which eventually lead the weldment to failure. This is due to the lowest mechanical performance of the FZ (Fig. 7), and to the larger deformation of the TWIP side with respect to the TRIP side (see Fig.18) These two concurring effects trigger a sort of necking where further localized deformation can develop up to final fracture. Moreover, relevant strain gradients are in the transition zones between the FZ, HAZs, and base materials, particularly at the TWIP side. These gradients are a source of undesirable stress concentrations.

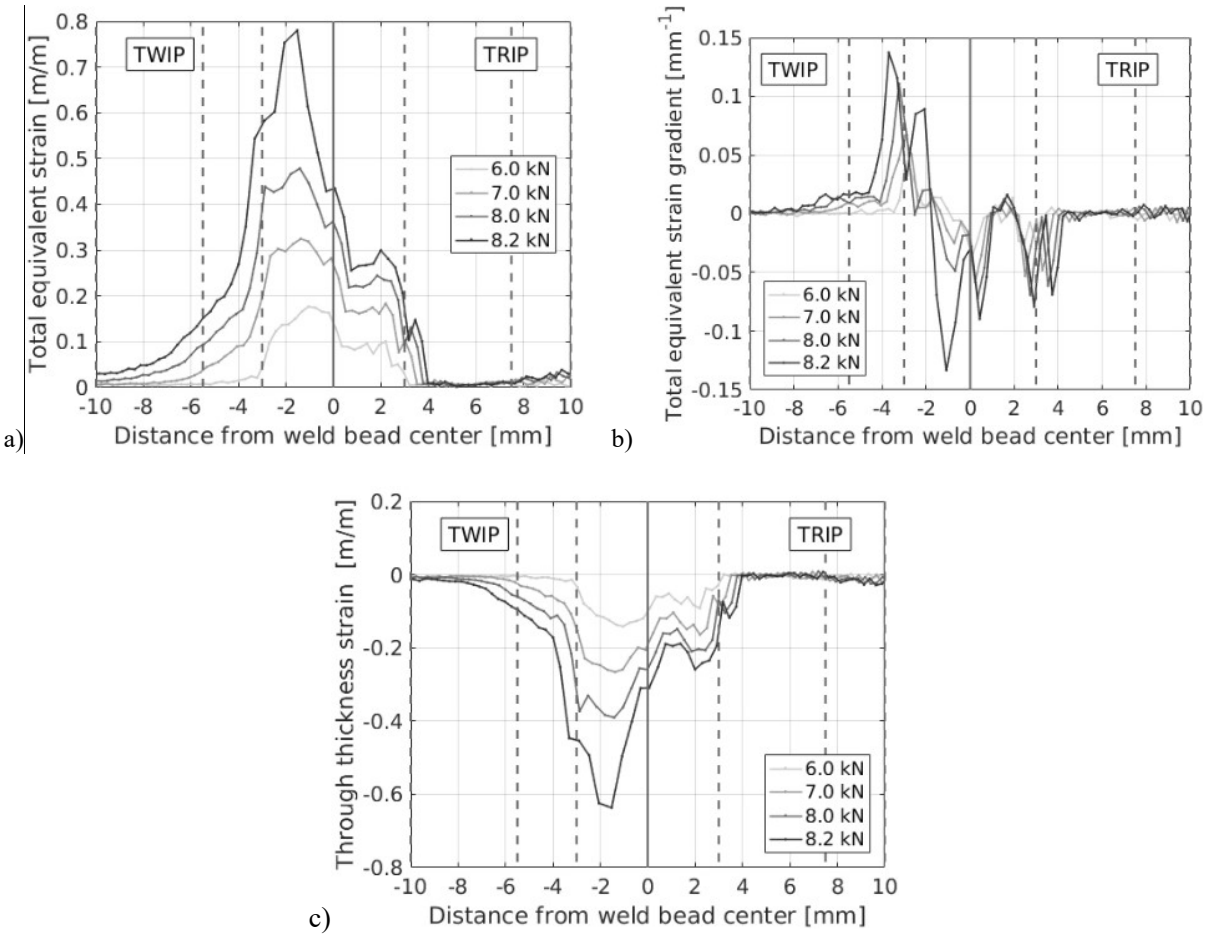

Fig. 18. Macro-specimen DIC results: a) total equivalent strain; b) total equivalent strain gradient; c) through-thickness strain. Data refer to the longitudinal central path of the macro-specimen.

A more effective formability index of TWIP-TRIP joints can be provided by normalizing the total equivalent strain measured on the macro-samples (Fig. 18a) to the uniaxial elongation at fracture of each zone it refers to (base metals, HAZs, FZ), as reported in Table 2. Such scalar quantity can be regarded as a material usage indicator, its value being proportional to the material exploitation during plastic deformation. In an ideal weldment, it would be favorable to have a constant and high material usage index throughout the whole joint, with the maximum values depending on the required process and in-service safety factor: a constant value throughout the joint would indeed mean limited strain gradients and consequently lower stresses, while high values would be representative of the capacity of the material to undergo significant plastic deformation, i.e. to be formable. Fig. 19 shows the material usage index at 8.2 kN load stage (close to fracture) along the same axial path of Fig. 18. Although the material usage

index is not uniform in the welded zone, values in a 0.3-1.0 range suggest that the different regions of the weldment are profitably exploited and participate to plastic deformations.

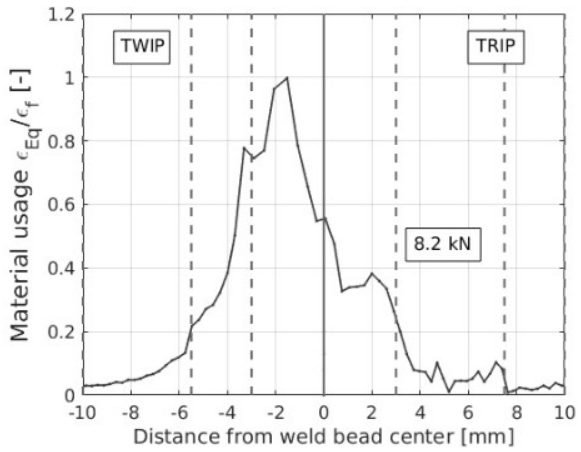

Fig. 19. Material usage index in the TWB weldment computed at 8.2 kN load level.

4. Conclusions

This study has investigated the possibility of using TWBs made of innovative TWIP and TRIP steels to fabricate tailored car parts. Accurate data about the mechanical behavior of the TWB weldments during plastic deformation have been provided. In this regard, the elasto-plastic constitutive laws of the FZ and HAZs (at the two steel sides) of the weld beads have been assessed in terms of formability and strength by tensile tests executed on micro-samples extracted from the different regions of the welded joints.

The major findings of this work can be summarized as follows:

- TWIP HAZ has a less hardness than base metal, and less grain coarsening than the HAZ at the TRIP side. The TRIP side HAZ exhibits a higher hardness than the base metal due to the presence of bainite and martensitic structures. Accordingly to these microstructures, different plastic behaviors have been highlighted from the stress strain curves obtained from the micro-samples. This inhomogeneity has also been confirmed by Vickers microhardness measurements.

- The elongation at fracture of the HAZ at the TWIP side and of the FZ are higher than the TWIP base metals. However, yield and tensile strength are significantly lower. This can be mainly attributed to the larger grains of these regions. Moreover, the dilution of the filler and steels limits the maximum achievable strength in the FZ.

- DIC analysis has shown that the fusion region exhibits an uneven plastic deformation throughout the gage length because of the inhomogeneous microstructure of the FZ and HAZs. This effect is also confirmed by the thickness variations of the micro-samples near the fracture surfaces.
- The inhomogeneous plastic behavior of the fusion zone add difficulties to model the thinning of the TWB weldment during a sheet forming operation. On the contrary, the HAZs at the TWIP and TRIP side show a more even elasto-plastic behavior.
- A local formability index of the TWIP-TRIP joints has been proposed, as the total equivalent strain normalized to the uniaxial elongation at fracture. Based on this factor, TWBs made of TWIP and TRIP steels have proved a good formability, such that they could be effectively employed in the fabrication of tailored automotive parts, even though the use of an austenitic filler wire is always mandatory.

Overall, sound constitutive material data have been obtained from the micro-sample tests. The information which has been provided allows to set up accurate numerical simulations of stamping of TWBs and, in turn, allows to better exploit the potential of tailoring complex and lighter parts and help to design a stamping processes efficiently. However, the numerical modeling of the FZ of a TWB weldment remains a hard task.

References

[1] Shome M, Tumuluru M (2015) Welding and joining of advanced high strength steels (AHSS). Woodhead Publishing, England.

[2] Russo Spena P, De Maddis M, D'Antonio G, Lombardi F (2016) Weldability and monitoring of resistance spot welding of Q&P and TRIP steels. Metals 6(11): art. n. 270. https://doi.org/10.3390/met6110270.

[3] Russo Spena P, De Maddis M, Lombardi F, Rossini M (2016) Dissimilar resistance spot welding of Q&P and TWIP steel sheets. Mater Manuf Proc 31(3): 291–299. https://doi.org/10.1080/10426914.2015.1048476.

[4] Májlinger K, Kalácska E, Russo Spena P (2016) Gas metal arc welding of dissimilar AHSS sheets. Mater Des 109: 615–621. https://doi.org/10.1016/j.matdes.2016.07.084.

[5] Mazar Atabaki M, Ma J, Liu W, Kovacevic R (2015) Hybrid laser/arc welding of advanced high strength steel to aluminum alloy by using structural transition insert. Mater Des 75: 120–135. https://doi.org/10.1016/j.matdes.2015.03.022.

[6] Alipooramirabad H, Paradowska A, Ghomashchi R, Reid M (2017) Investigating the effects of welding process on residual stresses, microstructure and mechanical properties in HSLA steel welds. J Manuf Proc 28: 70–81. https://doi.org/10.1016/j.jmapro.2017.04.030.

[7] Kouadri-Henni A (2017) Effect of welding laser process on macrostructures and the mechanical properties of coating steel DP600: Influence of vaporization zinc. J Manuf Proc 30: 83–96. https://doi.org/10.1016/j.jmapro.2017.07.025.

[8] Liu, W, Ma J, Yang G, Kovacevic R (2014) Hybrid laser-arc welding of advanced high-strength steel. J Mater Proc Technol 12: 2823–2833. https://doi.org/10.1016/j.jmatprotec.2014.06.018.

[9] Saha DC, Westerbaan D, Nayak SS, Biro E, Gerlich AP, Zhou Y (2014) Microstructure-properties correlation in fiber laser welding of dual-phase and HSLA steels. Mater Sci Eng A 607: 445–453. https://doi.org/10.1016/j.msea.2014.04.034.

[10] Bayraktar E, Kaplan D, Yilbas BS (2008) Comparative study: mechanical and metallurgical aspects of tailored welded blanks (TWBs). J Mater Proc Technol 204(1–3): 440–450. https://doi.org/10.1016/j.jmatprotec.2007.11.088.

[11] Gong H, Wang S, Knysh P, Korkolis YP (2016) Experimental investigation of the mechanical response of laser-welded dissimilar blanks from advanced- and ultra-high-strength steels. Mater Des 90: 1115–1123. https://doi.org/10.1016/j.matdes.2015.11.057.

[12] Padmanabhan R, Baptista AJ, Oliveira MC, Menezes LF (2007) Effect of anisotropy on the deep-drawing of mild steel and dual-phase steel tailor-welded blanks. J Mater Proc Technol 184: 288–293. https://doi.org/10.1016/j.jmatprotec.2006.11.051.

[13] Panda SK, Ravi Kumar D (2010) Experimental and numerical studies on the forming behavior of tailor welded steel sheets in biaxial stretch forming. Mater Des 31(3): 1365–1383. https://doi.org/10.1016/j.matdes.2009.08.046.

[14] Xu F, Sun G, Li G, Li Q (2014) Experimental investigation on high strength steel (HSS) tailor-welded blanks (TWBs). J Mater Proc Technol 214(4): 925–935. https://doi.org/10.1016/j.jmatprotec.2013.11.018.

[15] Kangn H, Cho L, Lee C, De Cooman BC (2016) Zn penetration in liquid metal embrittled TWIP steel. Met Mater Trans A: Phys Met Mater Sci 47(6): 2885–2905. https://doi.org/101007/s11661-016-3475-x.

[16] Beal C, Kleber X, Fabregue D, Bouzekri M (2012) Embrittlement of a zinc coated high manganese TWIP steel. Mater Sci Eng A 543: 76–83. https://doi.org/101016/jmsea201202049.

[17] Rossini M, Russo Spena P, Cortese L, Matteis P, Firrao D (2015) Investigation on dissimilar laser welding of advanced high strength steel sheets for the automotive industry. Mater Sci Eng A 628: 288–296. https://doi.org/101016/jmsea201501037.

[18] Wang T, Zhang M, Xiong W, Liu R, Shi W, Li L (2105) Microstructure and tensile properties of the laser welded TWIP steel and the deformation behavior of the FZ. Mater Des 83: 103-111. https://doi.org/101016/jmatdes201506002.

[19] Nguyen NT, Hariharan K, Barlat F, Lee MG (2014) Design of high strength differential TWB to enhance drawability: FE study and optimization. Int J Precis Eng Manuf 15(11): 2273–2283. https://doi.org/101007/s12541-014-0591-7.

[20] Nguyen NT, Hariharan K, Chakraborti N, Barlat F, Lee MG (2015) Springback reduction in tailor welded blank with high strength differential by using multi-objective evolutionary and genetic algorithms. Steel Res Int 86(11), 1391–1402. https://doi.org/101002/srin201400263.

[21] Broggiato GB, Cortese L (2009) White-light speckle image correlation applied to large-strain material characterization. European J Comput Mech 18(3-4): 377-392.

[22] Broggiato GB, Campana F, Cortese L, Mancini E (2012) Comparison between two experimental procedures for cyclic plastic characterization of high strength steel sheets. J Eng Mater Technol 134(4), art no 041008.

[23] EN ISO 643, 2012 Micrographic determination of the apparent grain size International Standard of Organization (ISO), CP 401 - 1214 Vernier, Geneva, Switzerland.

[24] ASTM E384, 2017 Standard Test Method for Microindentation Hardness of Materials, ASTM International, 100 Barr Harbor Drive, PO Box C700, West Conshohocken, PA, 19428–2959 USA.

[25] ASTM E8 / E8M, 2013 Standard Test Methods for Tension Testing of Metallic Materials, ASTM International, 100 Barr Harbor Drive, PO Box C700, West Conshohocken, PA, 19428–2959 USA.

[26] Hall EO (1951) The deformation and ageing of mild steel: III discussion of results. Proc Phys Soc London B64, 747.

[27] Petch NJ (1953) The cleavage strength of polycrystals. J Iron Steel Inst 174: 25–28.

[28] Gutierrez-Urrutia I, Raabe D (2012) Grain size effect on strain hardening in twinning-induced plasticity steels, Scripta Mater 66: 992–996. https://doi.org/101016/jscriptamat201201037.

[29] De Cooman BC, Kwang-geun C, Jinkyung K (2011) High Mn TWIP steels for automotive applications. In: Chiaberge M (ed) New trends and developments in automotive system engineering, IntechOpen, Croatia, pp. 101-128. ISBN: 978-953-307-517-4.